BIOCHEMISTRY
including biophysical chemistry & molecular biology
Article

Biochemistry **2010,** *49,* 6247–6262 6247
DOI: 10.1021/bi100166x

Widespread but Small-Scale Changes in the Structural and Dynamic Properties of Vaccinia Virus Poly(A) Polymerase upon Association with Its Processivity Factor in Solution†

C.-Z. Li,‡ M. Koter,‡,§ X. Ye,‡ S.-F. Zhou,‡ W. Chou,‡ R. Luo,‡ and P. D. Gershon*,‡

‡*Department of Molecular Biology and Biochemistry, University of California, Irvine, California 92697.* §*Current address: Department of Biochemistry, Medical University of Warsaw, St., Banacha 1, Warsaw, Poland.*

Received February 3, 2010; Revised Manuscript Received May 6, 2010

ABSTRACT: Vaccinia virus poly(A) polymerase (VP55) has been analyzed via hydrogen−deuterium exchange (HDX) mass spectrometry in the absence and presence of its processivity factor, VP39, to improve our understanding of the mechanism by which processivity is impressed on the polymerase. For 119 peptic peptides covering 74.1% of VP55, the extent of HDX at 900 s was interpreted in the context of parameters deduced from the VP55−VP39 X-ray crystal structure. While HDX exhibited a degree of correlation with the mean SASA of whole residues within each peptide segment, HDX was generally more active than expected from either the SASA or hydrogen bonding status of the exchangeable amide proton, indicating a significant molecular dynamics contribution to amide proton deprotection. Peptic peptides undergoing either more or less HDX than expected were distributed throughout VP55 and showed consistency between multiple overlapping peptides. VP39 had a net, marginal cooling effect on VP55, indicating a possible restriction of VP55's flexibility. VP39's cooling effect was most extensive within the central domain of VP55's three domains, while a patch within VP55's C-terminal domain showed an increased level of HDX in the presence of VP39. Langevin dynamics all-atom simulations of VP55 motions showed slower relaxation to equilibrium in the absence of VP39. At equilibrium, regions showing extremes of variation in simulated atomic fluctuation were localized within VP55's N- and C-terminal domains, and VP39 had a predominantly cooling effect on VP55. Broadly, across VP55's peptic peptides, a mild negative correlation was noted between the extent to which deuteration was more active than predicted from the structure and the amplitudes of the simulated atomic fluctuation and/or degree of disorder at equilibrium.

Vaccinia virus protein VP55 is a poly(A) polymerase (PAP) that adds ∼30-nucleotide poly(A) tails to mRNA 3′ ends in vivo and to permissive primers in vitro, in a rapid processive burst of polyadenylation, before dissociating from the primer (*1*, *2*). A unique feature of VP55 is its ability to translocate, unaided, with respect to single-stranded nucleic acid while extending the 3′ terminus (*3*, *4*). VP55 translocation continues until the enzyme has locomoted, fully, from the 33−34-nucleotide uridylate-rich initial primer for which it has affinity to the nascent oligo(A) tail with which it is unable to interact stably, leading to the cessation of the rapid processive polyadenylation burst. VP55 forms a 1:1 heterodimer (*1*) with a single-domain processivity factor (VP39) (*5*, *6*), and the VP55−VP39 heterodimer can processively elongate poly(A) tails far beyond VP55's 30-adenylate length limit. VP39 is not a poly(A) binding protein per se, though within the VP55−VP39 heterodimer, VP55's strong discrimination against uridylate-lacking primers is abrogated (*7*).

While there is no crystal structure available for monomeric VP55, prompting the current study, a 2.3 Å resolution X-ray crystal for the VP55−VP39 heterodimer has been reported (*8*) showing VP55 to have three domains, of which the central one contains the polymerase catalytic center. Within the heterodimer, VP55 has a bilobal ("kidney bean") topology in which VP39 appears to nestle within the indentation. Although the complete path of the primer around the polymerase is unknown, the three key sites of VP55−primer interaction known to be critical to productive interaction (*9*, *10*) were recently identified on VP55's surface in crystallographic soaking experiments (*11*). The three sites are the catalytic center (containing the 3′-terminal trinucleotide of the primer), the proximity of residue I477 (contacting a single rU at approximately primer position −9), and the proximity of residue F47 (contacting rUrU at primer positions −26 and −27) (*10*, *11*). Side chain substitutions at the F47 site compromised the extension of tails beyond a length of ∼12 nucleotides by VP55 alone, but not the extension of poly(A) by the heterodimer (*11*), indicating that primer may be routed away from this site within the heterodimer. Using fluorescence approaches, translocation of VP55 with respect to the primer was shown to be saltatory in character, with the polymerase−primer complex undergoing apparent isomerization at three or four specific transition points during its translocation cycle (*4*). For the VP55−VP39 heterodimer, however, no clear evidence of isomerization could be detected (unpublished). Whether the VP55-alone isomerization events are based primarily on primer dynamics or protein dynamics is unknown. However, crystallographic evidence exists for remotely triggered changes in local conformation within VP55 (*11*), and it would not seem unreasonable to also suppose that, during extension of the primer, which is

†This work was supported by National Institutes of Health Grant GM51953.

*To whom correspondence should be addressed. E-mail: pgershon@uci.edu. Phone: (949) 824-9606. Fax: (949) 824-8551.

Published on Web 05/14/2010

known to loop or wrap around the polymerase (*11*), the primer may also undergo conformational flexing.

If VP55 has inherent interdomain flexibility, permitting its flexing and/or facilitating conformational connectivity through the protein during its translocation, then models for the action of VP39 as a processivity factor may include either the remodeling of VP55 or the selection of a restricted conformation. Such an activity by VP39, in turn, may be expected to result in alterations in amide proton protection within VP55, not necessarily just in regions sequestered within the VP55−VP39 dimerization interface. The aims of this study were therefore twofold: (a) to understand the extent to which VP39 affects amide proton protection patterns within VP55 to gain insights into how VP39 acts as a processivity factor and (b) to address amide proton protection patterns within VP55 alone which, from the studies mentioned above, might be expected to have significant conformational flexibility.

In contrast to the demonstrable, independent dynamics of VP55 discussed above, VP39 is not considered a strong candidate for molecular dynamics during translocation of the VP55−VP39 heterodimer. First, unlike VP55, VP39 is a single-domain protein. Second, fluorescence data indicate that the heterodimer is more conformationally restricted than free VP55 (unpublished data), obviating a dynamic role for VP39 within the heterodimer. Third, crystal structures for monomeric VP39 are known (*5*, *6*, *12*) in addition to the known structure for VP39 within the heterodimer (*8*), and all structures for VP39 determined thus far are invariant with respect to one another (comprising a compact, single-domain protein in contrast to the three-domain, bilobal VP55).

Various investigators have established, over the past 40 or more years, that changes in the kinetics of solvent exchange occur at protein main chain amide protons in response to changes in protein environment or state, and that this may be a function of solvent penetration and/or local conformational changes, and/or small-amplitude dynamic fluctuations (*13*−*16*). HDX[1] has therefore become established as a tool for the investigation of protein structure and dynamics, and alterations therein. The use of mass spectrometry as opposed to NMR for the HDX studies has facilitated the sensitive detection of main chain amide deuteration levels, at moderate regiospecific resolution within the primary structure (*16*, *17*). Here, we have applied HDX by mass spectrometry (HDX-MS) to the study of VP55 in monomeric form, and changes therein upon binding VP39. To facilitate rapid and convenient nanoscale HDX-MS experiments with available instrumentation, the study was initiated by the development of a rapid nano-LC-MALDI approach. In separate experiments, Langevin dynamics simulations were performed on VP55 and on the VP55−VP39 heterodimer, and possible correlations between the experimental and simulation approaches are discussed.

EXPERIMENTAL PROCEDURES

Materials. Deuterium oxide (D_2O, 99.9%) was purchased from Cambridge Isotope laboratories, Inc. (Andover, MA), and immobilized pepsin was purchased from Pierce Chemicals (Rockford, IL). Bradykinin fragment 2-9 ammonium monobasic phosphate and α-cyano-4-hydroxycinnamic acid were purchased from Sigma (St. Louis, MO). The latter was recrystallized from ethanol before being used. 3-(*N*-Morpholino)propanesulfonic acid (MOPS) was purchased from United States Biochemical Corp. (Cleveland, OH). A 1 M MOPS stock solution was prepared by dissolving in D_2O, and then the pH was adjusted with NH_4OH to pH 7.0 (pD 7.4). CH_3CN and CH_3OH (LC−MS grade) were purchased from EMD Chemicals Inc. (Gibbstown, NJ). Water was Milli-Q grade (Millipore, Billerica, MA), and trifluoroacetic acid (TFA) was acquired from Applied Biosystems (Scoresby, Australia). The mass standards kit for MALDI plate calibration was obtained from Applied Biosystems (Foster City, CA). Dithiothreitol (DTT) was from Research Products International Inc. (Mt. Prospect, IL). Vaccinia proteins VP55-ΔN10 and VP39-ΔN26 were expressed in *Escherichia coli* and purified as described previously (*4*). Purified protein stocks in 10 mM Tris (pH 8.7), ∼75 mM NaCl, and 1 mM DTT (protein concentration above ∼4 mg/mL) were stored aliquoted. Matrix solution comprised αCHCA (3 mg/mL) freshly dissolved in 75% acetonitrile, and 0.1% TFA, 2 mM ammonium monobasic phosphate (final pH of 2.5 at 0 °C). For each experiment, matrix solution was freshly spiked with internal calibrant comprising Bradykinin fragment 2-9 (MH^+ = 904.468; final concentration of 100 fmol/mL). Pepsin (Sigma) was dissolved in phosphate buffer (pH 4.9) at a concentration of 10 mg/mL.

MS/MS. For MS/MS library-building experiments, 20 μL aliquots of the VP55 solution (0.4 mg/mL) were digested in five aliquots using immobilized pepsin (5, 10, 20, 30, and 40 μL of a 50% slurry) for 2 min before the samples were recombined. As an alternative to immobilized pepsin in some experiments, 4 μg of VP55 (4 mg/mL) was mixed with 9 μL of 50 mM (deuterated or water-based) MOPS buffer, quenched with ice-cold water adjusted to pH 2.5 with TFA, and then digested for 2 min with 5 μg of solution-phase pepsin at 0 °C. Samples were fractionated by integrated nano-LC with online robotic spotting (LC Packings, Amsterdam, The Netherlands), employing the FAMOS autoinjector, ULTIMATE and ULTIMATE PLUS pumps, a SWITCHOS solvent switching unit, a UV detector, and a PROBOT spotter. Peptides were fractionated over a 0.1 mm × 150 mm capillary C18 column (Michrom), with a 0.3 mm × 5 mm trap column (Dionex). Gradient solvents were A (98% H_2O, 2% CH_3CN, and 0.2% TFA) and B (85% CH_3CN, 5% 2-propanol, and 0.1% TFA). Online dosage with a matrix/internal calibrant mixture (Materials) was via the PROBOT dosage syringe, spotting onto Opti-TOF plates (AB-Sciex). Later, library supplementation experiments were conducted via manual nano-LC-MALDI fractionation as described for HDX experiments (below). MS/MS spectra were acquired for precursors in the m/z 600−3000 range using a model 4700 MALDI-TOF/TOF mass spectrometer (AB-Sciex, Foster City, CA). A vaccinia or vaccinia/human database was interrogated with MS/MS spectral peaklists from the resulting spectra using the MASCOT search engine [Matrix Science Ltd., London, U.K. (*18*)] with no enzyme specificity. Peptides scoring beyond a preset significance threshold ("Expect" < 0.05) were exported to a nonredundant peptide library using the development version of TOF2H macroset 1.1 (*19*) (http://tof2h.bio.uci.edu/). Multiple aliquots of undeuterated VP55 protein were digested with pepsin and then subjected to nano-LC-MALDI−MS/MS as described above, leading to progressive growth of the nonredundant library. The VP39 "decoy" library was built in a similar manner.

HDX Experiments. HDX experiments were performed in random order, and within each one, all time points were

[1]Abbreviations: SASA, solvent-accessible surface area; HDX, hydrogen−deuterium exchange; ESI, electrospray; XIC, extracted ion chromatogram; LC, liquid chromatography; MS, mass spectrometry; MALDI, matrix-assisted laser desorption ionization; % D, percent deuteration.

processed in random order. Prior to initiation of each HDX time point reaction, 20 μL of 50% immobilized pepsin slurry was washed twice with 1 mL of ice-cold protic 0.1% TFA (pH 2.5) followed by centrifugation (10000*g* for 2 min) and removal of the supernatant. To initiate an exchange reaction, 1 μL of VP55 (4 mg/mL) or a mixture comprising 1 μL of VP55 (4 mg/mL) and 2.3 μL VP39 (2 mg/mL) was diluted with 9 volumes of deuterated 50 mM MOPS buffer (pD 7.4) at room temperature. After deuterium exchange was allowed to proceed at room temperature for a specific time period (e.g., 0, 5, 10, 15, 30, 45, 60, 300, or 900 s), the reaction was quenched by addition of 9 volumes of ice-cold ~0.1% TFA in water (TFA concentration preadjusted, via a pH microelectrode, to bring a mock reaction mixture to pH 2.5). All subsequent steps were performed as rapidly as possible, on ice with centrifugation steps in a 4−5 °C coldroom. After the reaction had been quenched, the time point sample was immediately mixed with the 10 μL aliquot of immobilized pepsin prepared above and then incubated on ice for 2 min with occasional mixing. This was followed by centrifugation at 12000*g* for 5 s, either directly or through a Nanosep MF spindown filter (Pall LifeSciences, Ann Arbor, MI).

Peptides were fractionated in the coldroom using a capillary nano-LC-MALDI setup comprising a Waters (Waters Corp., Milford, MA) 600E HPLC multisolvent delivery system/controller (solvent A being 2% CH_3CN and 0.1% TFA in water and solvent B being 0.1% TFA in CH_3CN) connected via a splitter, to a standard injection valve/peptide trap (CapTrap cartridge, Michrom Bioresources, Auburn, CA)/switching valve arrangement and an analytical column comprising a Kasil-fritted fused silica capillary [0.25 mm (inside diameter) × 50 mm] packed with 2.7 μm C18 beads ("Halo", Mac-Mod Analytical Inc., Chadds Fort, PA). The column eluate was dosed with a matrix/internal calibrant solution (Materials) via a syringe pump (World Precision Instruments, Sarasota, FL)/microtee (Upchurch Scientific, Oak Harbor, WA). After manual injection of the pepsin-digested sample to the trap followed by a 3 min washing (solvent A, split flow rate of ~30 μL/min), peptides were resolved via a 5 min gradient from 15 to 40% solvent B (split flow rate of 8 μL/min), dosing with a matrix/calibrant mixture at a sample:matrix ratio of ~2:1. Outflow was manually spotted onto an Opti-TOF MALDI target plate seated in a plastic box on ice, at a rate of one spot per ~3 s, using as a time reference a metronome sound recorded on an iPod. After being spotted (typically ~132 spots), the plate was rapidly dried (20 s) using a < 50 mTorr vacuum generated by a two-stage VP100 pump (Thermo Savant, San Jose, CA) and then immediately docked in the 4700 MALDI TOF/TOF mass spectrometer. Positive ion mass spectra were recorded in reflectron/batch mode, in the m/z 600−3000 range with a focus mass of m/z 1500, accumulating 1000 laser shots per sample and calibrating each spot to the internal calibrant (Materials). The acquisition rate under these conditions was ~5.7 spots/min. To minimize sample-to-sample carryover between analyses, trap and analytical columns were washed between each experimental run, with a "triple sawtooth gradient" (1× 95% MeOH/0.1% TFA, 2× 95% CH_3CN/0.1% TFA), discarding the resulting eluate. The quality of washing was confirmed occasionally by running a blank sample.

The process described above was repeated for all time points in all experiments. Each experiment also included three controls: "F1H" (fully protic), in which a 15 s mock exchange step was initiated by dilution of VP55 into nondeuterated 50 mM MOPS buffer (pH 7.0); "0 sec", in which the protein sample was added to ice-cold quenching buffer followed by mixing with deuteric 50 mM MOPS; and "F2H", a fully deuterated control sample prepared by protein digestion with immobilized pepsin as described above, followed by lyophilization of the supernatant in a Freeze-Dry System/Freezone 4.5 (Labconco, Kansas City, MO) and then rehydration in deuterated 50 mM MOPS buffer (pD 7.4) at room temperature for 24 h. For "back-exchange" time points, the fully deuterated control was subjected to nano-LC-MALDI and fractions were allowed to remain on the plate for preset time periods prior to being vacuum dried and data being acquired.

HDX Data Processing. HDX experimental data were extracted from the 4700s Oracle database using T2DE (http://proteomecommons.org/tools.jsp#Data/Extraction/Tools). All subsequent steps were performed by TOF2H (*19*), using a peaklist deisotoping mass tolerance of 12 ppm, an interspot mass tolerance of 30 ppm, an interplate mass tolerance of 40 ppm, DI gradient factors of 1.0, IP gradient factors of 0, and a mean isotopic mass difference of 1.0049 Da. Adducts were disregarded, and IP mass matching to the theoretical mass was conducted. When experiments included VP39, this protein's refMPL was used as a search decoy. For spectral editing, primary and secondary mass tolerances for matching spectral peak apexes to peaklist values were 30 and 200 ppm (internal and default calibration, respectively), and T2DE 2.0-downloaded spectra were occasionally "snapped" to align monoisotopic peak apexes with peaklist values. EDITOR's recommendations with regard to acceptance or rejection of target isotope clusters from active fractions within XIC's were either allowed to proceed automatically or confirmed via user intervention. Isotope clusters were accepted or rejected on the basis of signal-to-noise ratios, association of the lightest visible peak with the peaklist monoisotopic or isotope progeny mass hit, and peak shape and spacing (good segregation from neighbors and/or superimposed clusters in all time points). Using TOF2H-Rates Browser, recorded rates were overlaid and averaged across replicate experiments, with and without back-exchange correction, with standard deviations calculated according to the population of centroid masses from all contributing individual spectral segments. Occasionally, TOF2H's inter/extrapolation function was used to infer the occasional missing time point in one of several overlaid rate plots. Curves for the entire study were globally "recontoured" to determine a deuteration level value representing an informative spread of transition time points. Colors were rendered on protein three-dimensional structure models (ribbon representation) using PyMol, molecular visualization software (DeLano Scientific, Palo Alto, CA). SASA (*20*) values were calculated for the amide proton of each peptide, after the latter's position had been modeled [using AMBER 9 (*19*)] on the basis of an effective proton radius of 1.00 Å and a water probe radius of 1.40 Å. SASA values were summed across each peptide and then divided by the number of backbone amide exchange-active residues, minus the N-terminal position.

Langevin Dynamics Simulations in Implicit Solvent. Simulations were all-atom (including hydrogens). The initial VP55 and VP55−VP39 structures were both taken from Protein Data Bank (PDB) entry 2GA9 (*8*), after the missing loops had been modeled using Modeller7 (*21*−*23*). To relax any possible clashes, initial modeled structures were minimized with a steepest descent minimization of 1000 steps using the AMBER 9 simulation package (*19*). To study the influence of VP39 on the VP55−VP39 binding interface, Langevin dynamics (LD) simulations were

Table 1: HDX Experiments with VP55 Alone and VP55 with VP39[a]

	VP55				VP55 with VP39			
	1	2	3	4	1	2	3	4
total no. of search hits	116	101	95	150	76	105	101	183
no. of unique edited peptides experiment-wide, no BE correction	39	50	44	72	42	30	41	69
no. of of peptides	28 (40.6% coverage)				13			
F2H mean	58.9% of theoretical maximum % D				64.3% of theoretical maximum % D			
F2H max	83.9% of theoretical maximum % D				76.5% of theoretical maximum % D			
F2H SD	14.58%				9.29%			

[a]Each HDX experiment (1−4) comprised nine forward exchange time points (F1H, 0, 5, 10, 15, 30, 45, 60, 300, and 900 s, and F2H), and three time points of back-exchange correction (300, 900, and 1800 s). In each experiment, HDX-MS peaklists from all F1H chromatographic fractions were combined and the combined list was searched against a 382-member library of MS/MS-confirmed VP55 peptic peptides. For VP55−VP39 heterodimer experiments, the search included a VP39 library as a decoy (*19*). Of the 119 peptides analyzed (Table S1 of the Supporting Information), deuterium uptake rate curves were generated for those in which data were available at all time points.

conducted with a low friction constant (also known as the solvent collision frequency, solvent viscosity, or γ) of 1 ps^{-1} for VP55 with and without VP39 in implicit solvent (*23*, *24*) using default parameters in the AMBER 9 simulation package (*19*). SHAKE (*24*) was activated for bonds containing hydrogen atoms, so that a time step of 2 fs could be used in the leapfrog (*25*) numerical integrator. After the sample had been heated for 20 ps from 0 to 298 K, the production run was performed for 7 ns at 298 K in the VP55-with-VP39 simulation and for 11 ns in the VP55-without-VP39 simulation. Mean structures were output for backbone atoms only (the positions of side chain atoms being distorted by structural averaging).

Scoring the Extent of Deviancy from a Direct Relationship between the SASA and Deuteration Rate. To calculate the "rates deviancy score" in plots of mean SASA versus transition time (e.g., in Figure 3B), the highest observed score on each axis was set to 100, and SASA transition time values for each plotted peptide were rescored according to each new axis. The rates deviancy score for each peptide was the sum of the two new scores. In this way, all values along the diagonal (e.g., in Figure 3B) equaled 100.

RESULTS

HDX by LC-MALDI: Resolution of Chromatographic Ambiguities. After a library of MS/MS-confirmed peptic peptides had been built (Experimental Procedures and Supporting Information), eight full HDX-MS experiments were performed by nano-LC-MALDI: four with VP55 alone and four with VP55 in combination with VP39. Plots of the rate of deuterium uptake versus time were built using TOF2H-EDITOR, and data for masses shared either between VP55-alone experiments or between VP55−VP39 experiments were averaged using TOF2H-RatesBrowser. In this way, HDX data of sufficient quality to clearly identify maximum deuteration levels were obtained for 119 peptides in one or both of the two sets of experiments (Table S1 of the Supporting Information). The identities of VP55 peptides in HDX experiments were established initially on the basis of mass matches to the MS/MS-confirmed peptide library. The potential for ambiguity in this process was addressed (Supporting Information).

HDX by LC-MALDI: Back-Exchange. For the assessment of back-exchange, a fully deuteric control "Timepoint" (F2H) was included in each experiment. For this pseudo-time point, peptic digests were subjected to exhaustive deuteration followed by the usual fractionation in protic solvents, spotting, mass spectrometry of the dried spots, XIC summation, and centroid mass determination (see Experimental Procedures). Table 1 shows global back-exchange data across the two sets of four experiments of the current study, for the subset of peptides for which all-time point deuterium uptake rates curves were later generated (see below). Mean F2H values were, for VP55 alone and VP55 and VP39, 58.9 and 64.3% of theoretical maximum deuteration, respectively, and were as high as 83.9 and 76.5%, respectively (Table 1). Comparable values were obtained, individually, for all peptides in Table S1 of the Supporting Information (data not shown). The residual values of ~36 and ~41% were considered to represent average values for back-exchange in the respective sets of experiments. This degree of back-exchange was not considered prohibitive to HDX experimentation (see Discussion). Attempts to further characterize back-exchange experimentally suggested that the bulk of BE occurred during LC steps (Supporting Information).

HDX of VP55 in Relation to Predicted Amide Proton Solvent Protection. For those peptides in Table S1 of the Supporting Information with data at the 900 s time point, the proportion of exchangeable protons remaining stable after deuteration for 900 s was plotted versus parameters deduced from crystallographic coordinates, namely, SASA, numbers of exchangeable amides that are hydrogen bonded, and numbers of hydrogen bonds (since some amide protons have two hydrogen bonds) (Figure 1). Two SASA calculations are shown, namely, SASA of the whole residue (Figure 1A) and SASA of the amide proton alone (Figure 1B). For the SASA of the whole residue (Figure 1A), a very weak correlation was observed between numbers of stable protons in the peptide and numbers of residues in the peptide having no predicted solvent exposure, as noted previously by others in other proteins (Discussion). A handful of peptides with low whole-residue SASA exposure were outliers with higher-than-expected apparent exchangeability (Figure 1A), indicating that, within the intact protein in solution, these peptides have a propensity for backbone amide deprotection that cannot be explained on the basis of the crystal structure. With regard to just the amide proton itself, there was no apparent correlation between the numbers of stable backbone amide protons and structural parameters (Figure 1B−D). In each instance, the plotted points for almost all peptides fell to the upper left of the proportionality line, indicating that, globally, VP55 in solution possessed fewer stable protons than the number that could be explained by analysis of SASA and hydrogen

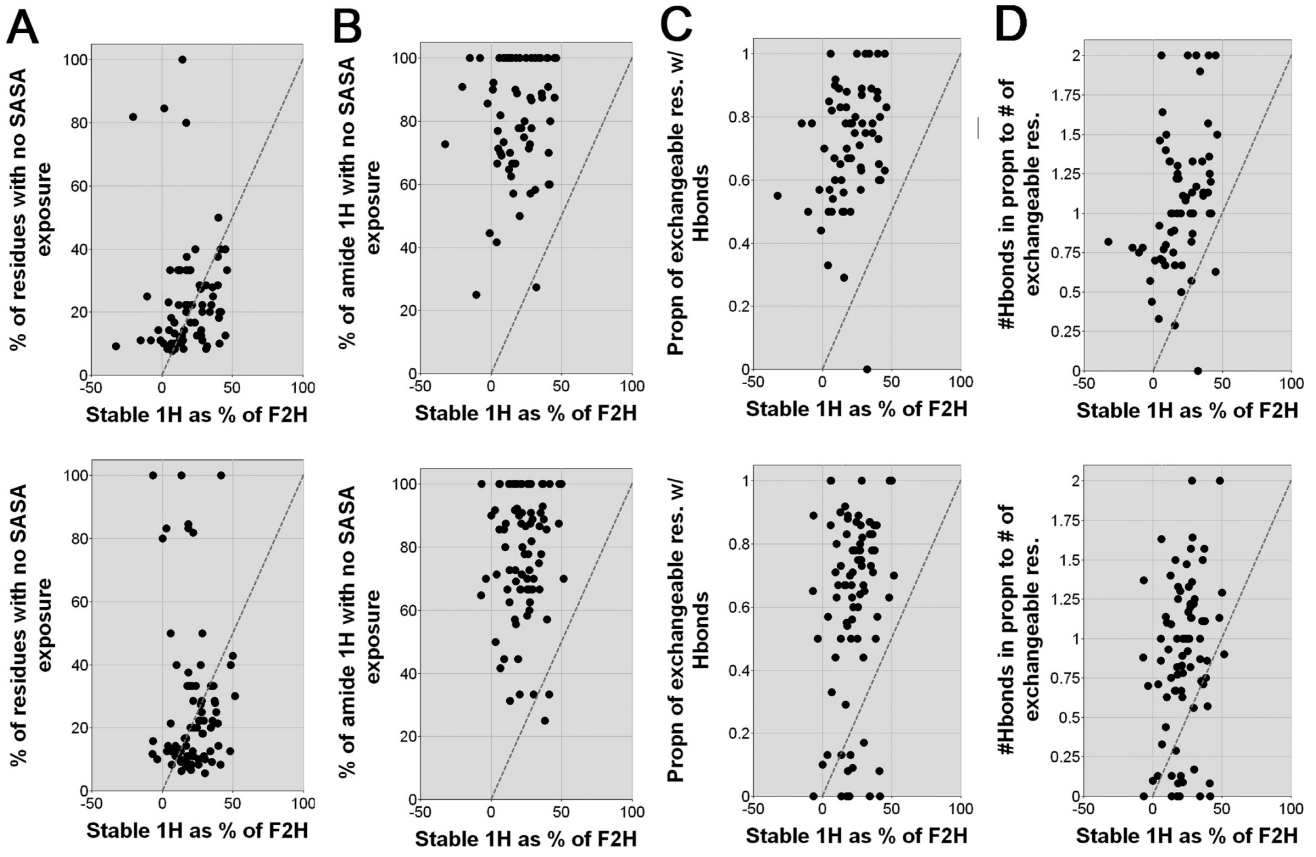

FIGURE 1: For the VP55 peptic peptides in Table S1 of the Supporting Information, amide protons in each peptide that remained unexchanged during the first 897 s of deuteration, indicated as a proportion of their fully deuterated (F2H) values, were plotted versus each of four structural parameters derived from the VP55−VP39 X-ray crystal structure. The dashed line indicates the prediction of proportionality between the extent of deuteration (*x* axis) and the given *y* parameter. The handful of negative values represent the few instances of the experimental % D exceeding that for F2H full deuteration within experimental error. All plots were generated automatically by TOF2H-RatesBrowser (*19*). Stable 1H at 897 s was calculated by interpolation between the 300 and 900 s time points. Peptides in Table S1 missing the F2H time point or whose coordinates were partially or completely missing in the crystal structure are not shown. Top four panels: VP55 alone data set (67 peptides). Bottom four panels: VP55-VP39 heterodimer (83 peptides). Although the peptide sets used for VP55 and VP55−VP39 analyses were not quite identical, the majority of observed differences in the plots arose from peptides common to both data sets. (A) *y* is the proportion of residues having exchangeable backbone amides in each peptide whose whole residue SASA equals 0 (no predicted exposure of the whole residue to solvent). (B) *y* is the proportion of exchangeable backbone amides in each peptide with a SASA of 0 (no predicted exposure of the amide proton to solvent). (C) *y* is the proportion of exchangeable backbone amides in the peptide that are hydrogen bonded in the crystal structure. Hydrogen bonds were calculated using the program "O". (D) *y* is the number of hydrogen bonds from exchangeable backbone amide protons in proportion to total numbers of exchangeable backbone amides (some amides formed two hydrogen bonds).

bonding within the static crystallographic structure. Therefore, in solution, backbone amide exchange deprotection was much more sensitive to exposure of the amide proton itself within the crystal structure than to exposure of the whole residue. In the presence of VP39 (Figure 1, bottom panels), the patterns described above were largely recapitulated; albeit, in the case of hydrogen bonding, "cooling" of some parts of the protein was apparent with respect to the data for VP55 alone (comparison of bottom and top panels).

Figure 2 shows the regiospecificity of each peptide in the HDX data set described above in relation to VP55's primary structure and tertiary structure as defined from crystallography of the VP55−VP39 heterodimer. For each peptide, the maximum percent deuteration is indicated as a proportion of either the mean SASA for the exchangeable amide protons of the peptide (Figure 2A) or the mean number of exchangeable amide protons within the peptide that are hydrogen bonded (Figure 2B). According to either analysis, some regions of VP55 were highly exchangeable (mobile) with respect to predictions from the heterodimer crystal structure (e.g., red or green regions) and others were relatively immobile (yellow or blue). Throughout the VP55 structure, helices were quite heavily represented within the more highly exchangeable set of peptides. Since the VP55 monomer crystal structure is unknown, the colored regions could be those that differ between the VP55 monomer and VP55 within the heterodimer and/or between VP55 in solution and VP55 *in crystallo*.

For 28 of the peptides from the VP55-alone HDX data set (Table S1 of the Supporting Information), data were obtained at all 11 time points. These peptides were therefore subjected to additional analysis on the basis of the full deuterium uptake rate curves (Figure 3) as opposed to the 900 s time point alone (above). All 28 plots (examples shown in Figure 3A) exhibited EX2 kinetics (*16*) consistent with solvent exposure of the peptide within the protein structure being extinguished faster than its amide protons can exchange. As a crude substitute for curve fitting, a "rate" value for each peptide was enumerated as the time required for the peptide to reach a specific deuteration level as a percentage of maximum experimental deuteration. The first time point at which deuteration exceeds this specific level is termed the "transition time point", and by interpolation, the time at which the deuteration level was exceeded is termed the "transition time". Separately, a SASA value for each of VP55's amide protons

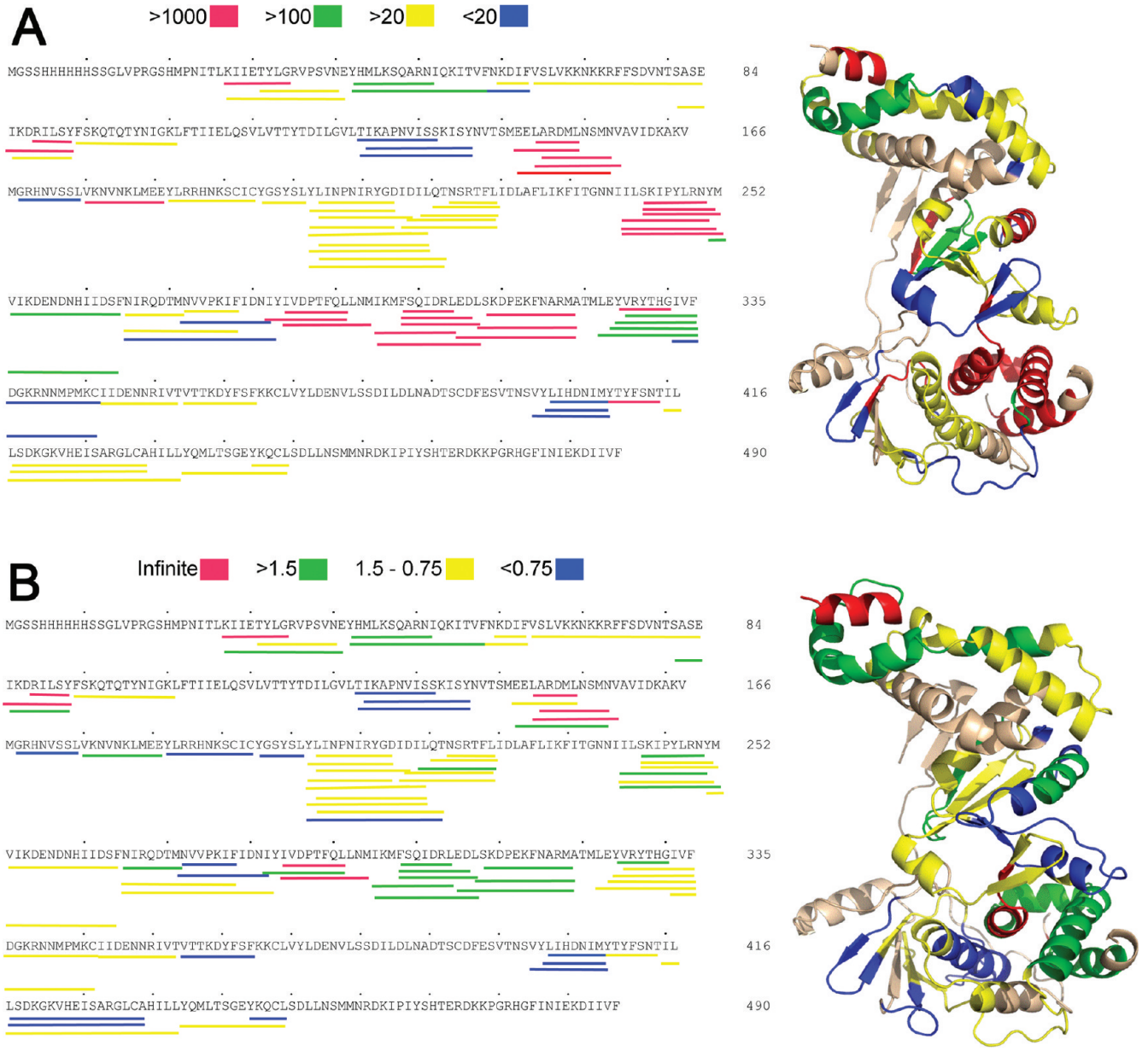

FIGURE 2: For the 82 peptides remaining in the VP55-alone data set after elimination of those that were scored as ambiguous (Table S1 of the Supporting Information), the sequence of VP55-ΔN10 (left panels) and the corresponding crystal structure [right panels (coordinates from ref *8*)] were marked up according to data columns from the "VP55 alone" section of Table S1. (A) According to Table S1 columns "Max. mean % D"/"mean SASA value", representing the % D of each peptide as a proportion of mean predicted solvent exposure for the exchangeable amide protons of the peptide (*x* value/*y* value in Figure 1A, top). A high value indicates a peptide with more deuteration than expected from theoretical solvent exposure. (B) From Table S1 column "Max. mean % D"/proportion of exchangeable residues free of H bonds, representing % D as a proportion of the mean number of exchangeable amide protons in the peptide that are non-hydrogen bonded in the crystal structure [*x* value/(1 − *y* value) from Figure 1C, top]. A high value indicates a peptide with more deuteration than expected from the number of amide protons predicted to be free of H bonds, and a low value indicates that non-hydrogen-bonded amides are not exchanging; 74% of VP55 was covered in the peptic peptides shown. The occasional occurrence of apparently contradictory colors in overlapping peptides represented, in nearly all instances, similar values falling just on either side of our imposed coloration boundary.

(i.e., their degree of predicted solvent exposure as opposed to the proportion of exchangeable protons showing any predicted SASA as in Figure 1B) was determined from the VP55−VP39 heterodimer crystal structure (*20*) [Experimental Procedures (removing coordinates for the nontarget subunit as done by Truhler et al. (*26*) in their examination of IkB in the absence of NfkB)]. In Figure 3B, transition times for each peptide were plotted against the average calculated degree of SASA for the peptide's exchangeable amide protons. Only a handful of the resulting points fell around the diagonal representing a correlation of greater predicted amide proton exposure with faster mean HDX (lower transition time); the majority of points fell significantly below the diagonal (average exchange faster than what would be expected from the mean amide proton exposure for the peptide). This reinforces the findings of Figure 2 (that were based simply upon nonexchanging protons as opposed to exchange rate), namely, that the majority of amide protons appeared more solvent accessible in solution than what was predicted from their conformations in the heterodimer crystal. In most instances, overlapping peptides in the primary structure (co-colored in Figure 3B) tended to cluster in the plot, lending confidence to the analysis. Even values in the orange and cyan groups in Figure 3B, which showed the least clustering, were within the same order of magnitude. Greater solvent accessibility than expected from the crystallographic coordinates might occur if

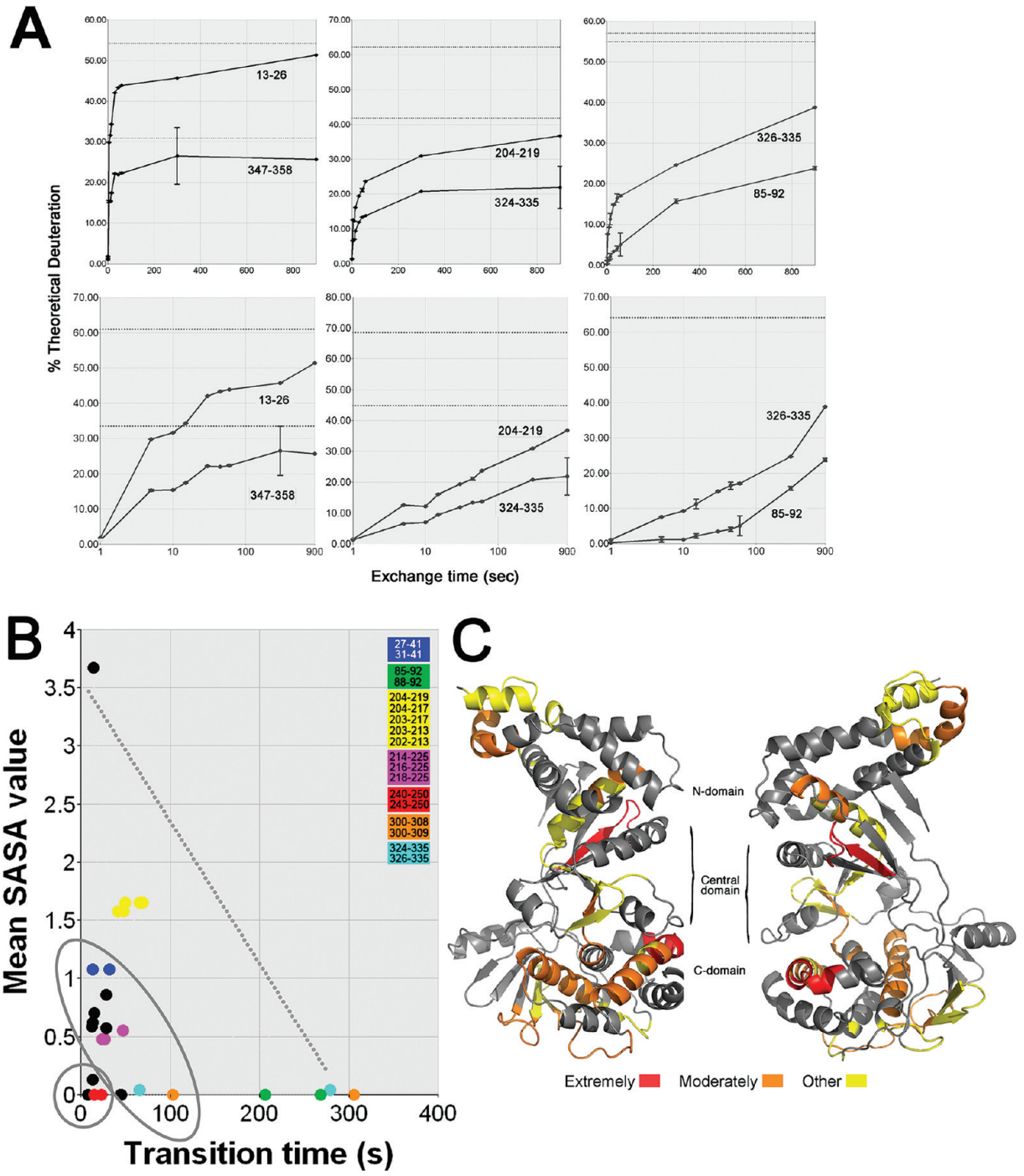

FIGURE 3: All-time point analyses of peptides from Table S1 of the Supporting Information (VP55 alone HDX data, without BE correction). (A) Sample deuterium uptake plots for peptides whose overall exchange rates were considered fast, medium, or slow. The top and bottom panels show times on linear and log scales, respectively. The left, center, and right panels shows values that are 50% of the maximum experimental time point deuteration reached within 5, 30, and 300 s, respectively. See Data Note 1 of the Supporting Information. Gray dotted lines show F2H values. Error bars are standard deviations. Peptides are identified by VP55 sequence end points. To generate plots, spectra were edited (to excise, sum, and centroid the relevant isotope clusters) using TOF2H-Editor (*19*) in semiautomated mode (i.e., with visual confirmation of software-isolated spectral segments prior to summing across XIC peaks and determination of centroid mass). TOF2H-RatesBrowser (*19*) was used to overlay deuterium uptake plots from equivalent peptides between replicate VP55-alone experiments and between replicate VP55−VP39 experiments. All overlays were averaged with attachment of error bars, and y axes were revised to the percent of theoretical deuteration [taking into account the nonexchangeability of the proline backbone nitrogen and the excessively rapid exchange of the N-terminal amide (*45*) and the backbone amide of the adjacent residue (*63*)]. (B) Mean SASA value for the amide proton vs the transition time for achieving 70% of the maximum experimental deuteration, for the 28 peptides for which uptake rate curves were complete at all 11 time points. Equivalent plots generated at various percentages of maximum experimental deuteration showed the same overall pattern. Groups of overlapping peptides in the sequence are colored according to the group of origin (color key in the plot). Black points could not be placed in a group. The gray dashed line represents the expectation of faster average deuteration of the peptide in proportion to greater solvent exposure. The line was placed such that zero SASA ($y = 0$) corresponds to peptides with the longest time to transition, and transition times tending toward zero ($x = 0$) correspond to peptides with the greatest SASA. (C) Peptides of panel B mapped onto the VP55 tertiary structure and colored according to the extent of deviancy from the dashed line in panel B: red for the most extremely deviant points in panel B, ringed with a circle; orange for moderately deviant points, ringed with an ellipse; and yellow for peptides represented by all other points in panel B. Two 180° rotations are shown.

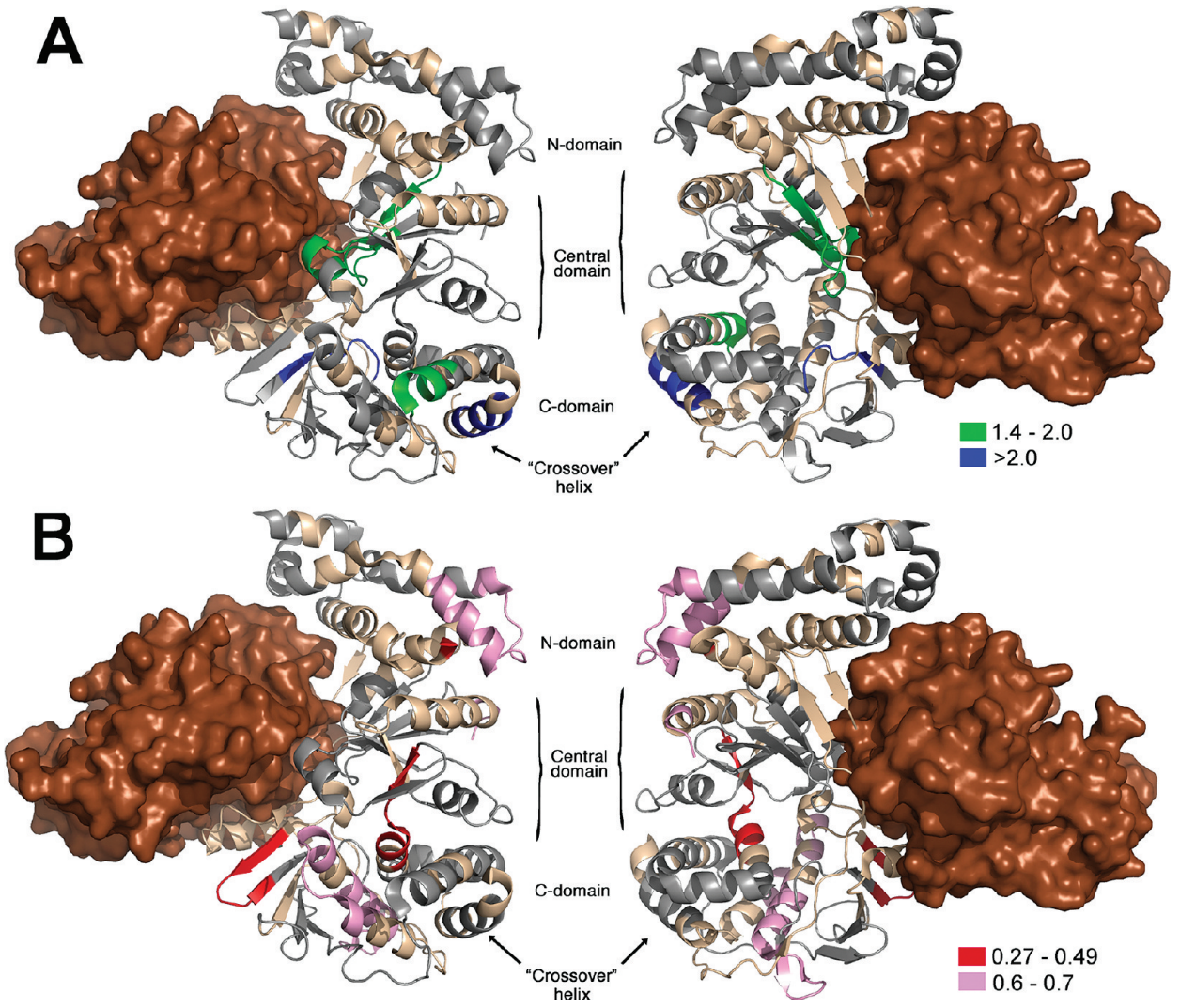

FIGURE 4: Effect of VP39 binding on VP55 in HDX experiments, represented as % D plot area (VP55/VP55−VP39) (Table S1 of the Supporting Information, right-hand column; see the text for details); 180° rotations of the heterodimer are shown: brown for VP39, wheat for regions of VP55 for which no data are available, and gray for regions of VP55 with ratios of 0.71−1.40, considered to have comparable % D in VP55 alone and in the heterodimer. (A) Regions of suppressed HDX in the presence of VP39: blue for ratios of >2.00, regarded as highly suppressed in the heterodimer; and green for ratios of 1.40−2.00, regarded as being moderately suppressed in the heterodimer. (B) Regions of enhanced HDX in the presence of VP39: pink for ratios of 0.50−0.71, considered to be moderately more exchangeable in the heterodimer; and red for ratios of 0.27−0.50, considered to be much more exchangeable in the heterodimer.

monomeric VP55 and the heterodimer (as crystallized) adopt distinct solution conformations or, perhaps more likely, from molecular dynamic considerations for VP55 in solution. To examine regiospecificity, the peptides in Figure 3B were divided into three sets, namely, nondeviant from the diagonal, moderately deviant, and highly deviant (the three groups ringed in Figure 3B). In Figure 3C, the segments of VP55's tertiary structure covered by these three sets of peptides are colored yellow, orange, and red, respectively. Colors were dispersed through the structure, indicating that various portions of VP55 are either structurally different in the monomer and in the VP55−VP39 heterodimer or susceptible to structural perturbations on a time scale of amide proton exchange.

Effect of VP39 on Deuterium Uptake by VP55. To predict the effect of VP39 on the solvent accessibility of VP55, SASA values were calculated for all of VP55's main chain amide protons in the heterodimer crystal structure before and after removal of VP39's coordinates, by rolling a solvent-size ball over both the monomer and the heterodimer. Only seven main chain amide protons of VP55 (those associated with residues Q259, D271, S378, D380, G465, R466, and H467) exhibited differences in predicted solvent accessibility. This perhaps arises because the interface is largely side chain-based.

Experimentally, a number of peptides in Table S1 of the Supporting Information yielded deuterium uptake data with both VP55 alone and the VP55−VP39 heterodimer. Their deuterium uptake curves are shown in Figure S2 of the Supporting Information. For each of these uptake curves, percent deuteration (% D) values at all common time points were summed (approximating the plotted area under the deuterium uptake curve, i.e., a combination of deuterium uptake rate and uptake extent during the experiment). A ratio of the resulting summed % D values [VP55: VP55−VP39 (Table S1 of the Supporting Information, right-hand column)] indicated the effect of VP39 upon amide protection within VP55. Among these ratios, the most marked were color-coded onto the three-dimensional structure of the heterodimer (Figure 4). Figure 4A shows regions of VP55 exhibiting markedly greater amide protection in the heterodimer, and Figure 4B shows regions of VP55 exhibiting markedly less amide protection. Although the experimental data set contained none of the seven

amides predicted to show VP39-dependent changes in predicted solvent accessibility, as calculated via SASA (above), the data were nonetheless informative. Regions within VP55's central domain closest to VP39 within the heterodimer exhibited noticeably increased amide protection in the presence of VP39 (Figure 4A). The central domain features the polymerase catalytic center along with the 3′ portion of the bound polyadenylation primer as it tracks away from the catalytic center.

Within VP55's C-terminal domain, various portions of a four-strand β platform close to the dimerization interface showed either increased (Figure 4A) or decreased (Figure 4B) levels of protection in the presence of VP39. This platform has been shown, by crystallography, to undergo extensive collapse and rearrangement upon the binding of segments of nucleic acids by the heterodimer (*11*). Apparently, therefore, comparable rearrangements can also occur upon the transition of VP55 from monomer to heterodimer, though a VP55 monomer crystal structure is not currently available for confirmation of this. Portions of additional helices and loops within the C-terminal domain also showed decreased levels of protection in the presence of VP39 (Figure 4B). The so-called "crossover helix" of VP55, a structural element of VP55 that is contiguous with the N-terminal domain in VP55's primary structure but which folds over into the C-terminal domain in VP55's tertiary structure, showed an increased level of protection as did an immediately adjacent helix (Figure 4A). The crossover helix is attached to the N-terminal domain via long connecting loops that could not be resolved within the crystallographic electron density but which presumably stretch across VP55's central domain. Within VP55's N-terminal domain, portions of helices distal from the interface with VP39 showed decreased levels of protection in the presence of VP39 (Figure 4B). Analysis of peptides from the two data sets (VP55 alone and heterodimer) that were not shared but that nonetheless overlapped with the shared peptides (data not shown) supported the data shown in Figure 4.

We conclude that VP39's interaction with VP55 not only leads to amide protection in and around the dimerization interface region of VP55 but also adjusts VP55's wider conformation sufficiently for changes in amide proton protection and deprotection to be detected throughout VP55. VP39-dependent changes in amide protection within VP55 could be attributable to hydrogen bonding changes (*27*), changes in the degree of "burial" of VP55 elements, and/or additional factors (below). These widespread effects VP55's local conformation notwithstanding, large, concentrated hotspots of VP39-dependent change in HDX suggestive of large scale domain movements were lacking.

Molecular Dynamics Simulation and Correlation of Simulation Parameters. To complement the experimental (HDX) approach, molecular dynamics simulations were performed. The VP55−VP39 heterodimer (*8*) and VP55 alone were each subjected to an all-atom Langevin dynamics simulation using the crystallographic coordinates as a starting point. Figure 5A shows the evolution of the two simulations as the time-dependent mean positional shifts [root-mean-square deviation (rmsd)] of all main chain atoms of VP55, from their starting positions. Within the heterodimer, VP55 relaxed to an equilibrium position within approximately 2.5 ns. In the absence of VP39, however, a significantly longer time (~6−7 ns) was required, indicating that the crystallographic coordinates for VP55 within the heterodimer are a more distant fit to the Langevian equilibrium conformation of monomeric VP55. Figure 5B shows differences between VP55's starting and ending conformations (in the presence

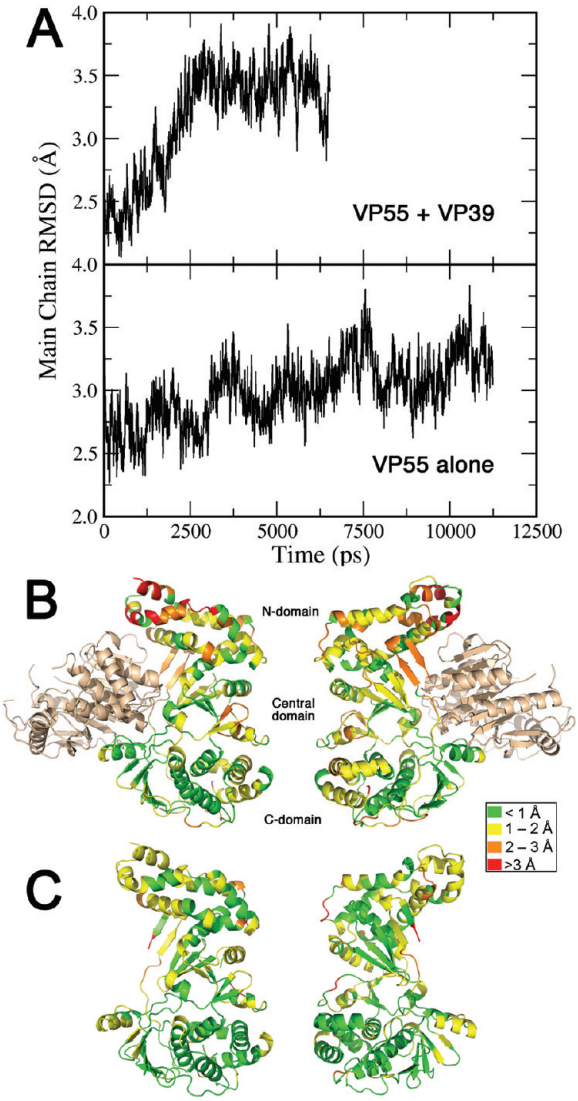

FIGURE 5: Langevin dynamics simulations of VP55 (all atoms) in the presence and absence of VP39−rmsd displacement. The crystallographic coordinates of VP55 within the heterodimer crystal were used as a starting point. (A) Plots show progression of the two simulations as the average of all main chain positional shifts from their starting positions. (B) VP55 structure indicating, for VP55 within the heterodimer, differences between the initial structure and the equilibrium position reached toward the end of the simulation: green for a < 1 Å difference, yellow for a 1−2 Å difference, orange for a 2−3 Å difference, red for a > 3 Å difference, and gold for the VP39 chain. Two 180° rotations are shown. (C) VP55 structure indicating residue-by-residue differences between the mean equilibrium positions of VP55 main chain atoms in the absence and presence of VP39, at equilibrium. Colors and orientations are like those in panel B.

of VP39) for the simulation. Structural elements throughout the protein shifted their position during simulation, movements in the N-terminal domain being the most significant. Figure 5C shows differences between VP55's simulated equilibrium conformations in the presence and absence of VP39. Differences were distributed throughout the protein, the most substantial of which were in loops and at the ends of some helices. Among these were loops and helices that also exhibited VP39-dependent changes in deuteration experimentally (Figure 4). Although the simulations were conducted, nominally, on the nanosecond time scale, implicit solvent was used for modeling along with a low solvent collision frequency (1 ps^{-1}). Such conditions have successfully modeled events that have been

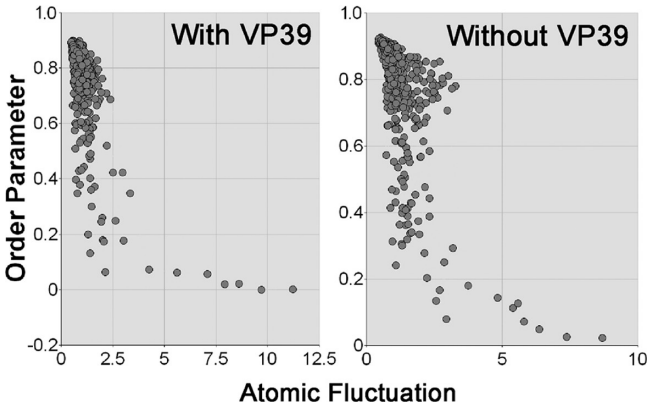

FIGURE 6: Langevin dynamics simulation: Correlation of mean atomic fluctuation with mean order parameter for all VP55 residues, over the final 4 ns of each of the two simulation trajectories shown in Figure 5A. For 77 and 76% of residues (in the absence and presence of VP39, respectively), increased atomic fluctuation with respect to the preceding residue correlated with decreased order. The value plotted for each residue is the mean of values for its main chain atoms.

shown, experimentally, to occur on time scales of microseconds to milliseconds (*28*, *29*), which is the time scale of protein motions that are characteristic of HDX with EX2 kinetics (see Discussion).

Differences between the two equilibrium structures resulting from Langevin dynamics simulation were next examined on a per-residue basis. In each of the two simulations, the atomic fluctuation (extent of rms standard deviation fluctuation of atoms from their mean positions) and order parameter (degree of disorder, as would be detected by NMR, for example) were recorded for the main chain atoms of all residues over the final 4 ns of simulation (i.e., after equilibrium had been reached). The atomic fluctuation and order parameter for each residue showed good inverse correlations (Figure 6; left and right panels derived from the trajectories shown in the top and bottom panels of Figure 5A, respectively), consistent with the expression of disorder as, broadly, the fluctuation of atoms.

Figure 7A shows the rms atomic fluctuation parameter, residue by residue, for VP55 backbone atoms in the two simulations (in the absence or presence of VP39). In each of the two traces, residue-to-residue variation was considerable. Notable spikes in the traces were mapped onto the VP55 crystallographic structure first by calculation of the per-residue rmsd fluctuation as a proportion of the mean value for all residues of VP55 in the same trace and then identification of clusters of residues at least two amino acids in length whose atomic fluctuation values exceeded the mean by at least ±50%. Panels B and C of Figure 7 show the positions of spikes in the atomic fluctuation for VP55-alone and VP55−VP39 simulations, respectively. On the time scale of the simulations, the "hottest" (red) and "coolest" (blue) regions of the backbone were concentrated markedly within VP55's N- and C-terminal domains regardless of whether VP39 was bound, with no extremes of flexibility obvious within the central domain. It may therefore be inferred that secondary structural elements in the N- and C-terminal domains have the most extreme dynamic or vibrational modes. The two traces of Figure 7A were compared with one another by calculation of a mean between the two traces, and then residues whose atomic fluctuation exceeded the mean by >20% in either trace were scored. All clusters of such residues at least two amino acids in length are indicated in Figure 7D. This figure indicates that the interaction of VP55 with VP39 resulted in changes in the

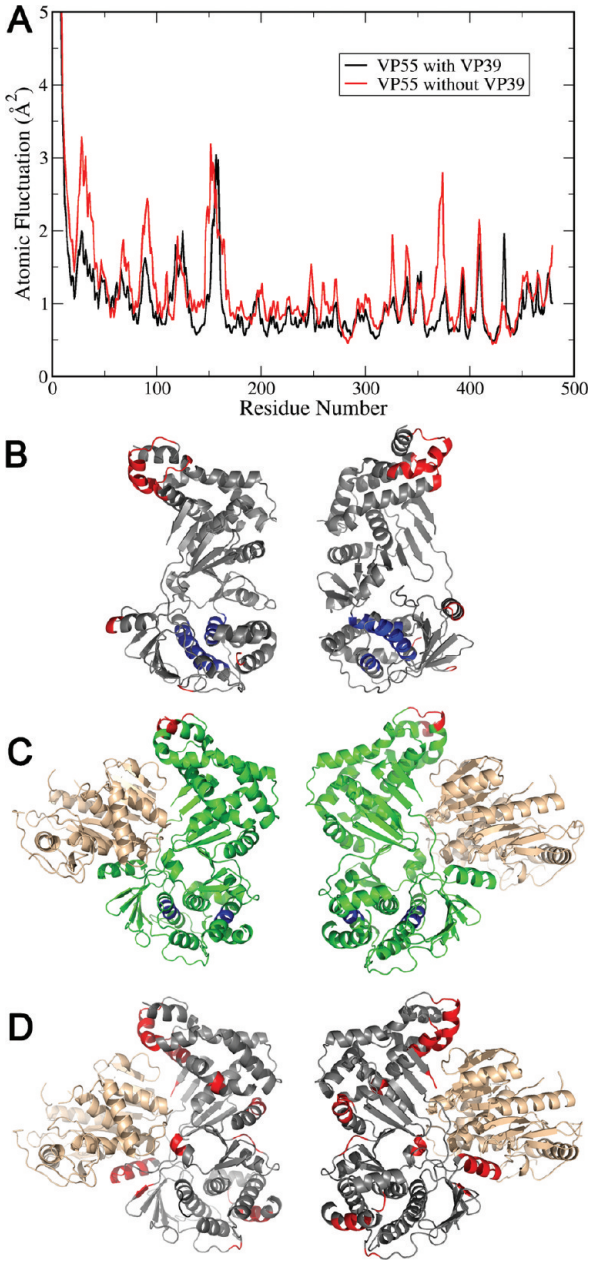

FIGURE 7: Langevin dynamics simulation: Analysis of the simulated atomic fluctuation on a per-residue basis. Values were computed from the final 4 ns of each trajectory (after equilibration). (A) Residue-by-residue plot. (B) From the "VP55 without VP39" simulation (panel A). Clusters of VP55 residues at least two amino acids in length whose atomic fluctuation values exceeded the mean for all residues by at least ±50%, mapped onto VP55's tertiary structure (two views of 180° rotations). The mean in this case was 1.295. Red regions are local clusters of at least two residues whose individual fluctuations exceed the mean for all residues of the polypeptide chain by >1.5 fold. Blue regions are local clusters of at least two residues whose individual fluctuations were less than half of the mean for all residues of the polypeptide chain. Gray regions are other regions of VP55. One of the more pronounced spikes in atomic fluctuation (residues ~150−160) fell across a crystallographically invisible loop of VP55 (*8*). (C) Same as panel B but for the "VP55 with VP39" simulation. The mean in this case was 1.103. Other regions of VP55 are, in this case, colored green not gray. The wheat chain is VP39. (D) Comparison of VP55 vs the heterodimer in terms of atomic fluctuation. Colored regions show sections in which trajectories for monomeric or VP39-associated VP55 deviated from the combined mean by ≥20%. Red indicates that monomeric VP55 exceeds the mean. Black indicates that the heterodimer exceeds the mean (there are not many black regions). Gray indicates other regions of VP55. The wheat chain is VP39.

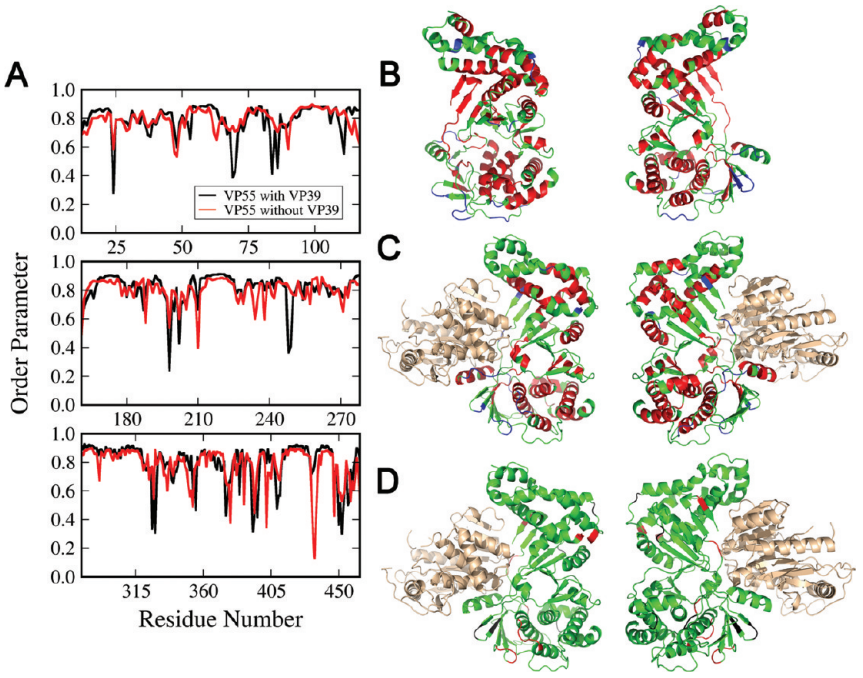

FIGURE 8: Langevin dynamics simulation: Analysis of simulated order parameter on a per-residue basis. (A) Residue-by-residue plots (split into three plots, representing the three defined domains of VP55, for easy viewing because of the narrowness of the spikes). (B−D) Same as panels B−D of Figure 7, except simulated order parameter instead of atomic fluctuation. The overall scheme, including the colors, is equivalent to that described for Figure 7 (green for other regions of VP55 in each case), except that the threshold value was 10%, not 50%. The mean for VP55 alone was 0.766, and for VP55 with VP39 was 0.761.

simulated backbone fluctuation within localized regions scattered throughout VP55. This global distribution of local effects within VP55 may result from VP39's interaction with each of VP55's three domains (*8*). According to the atomic fluctuation parameter, changes due to VP39 were predominantly in the direction of cooling.

Figure 8 shows an analysis equivalent to that of Figure 7, only for order parameter instead of atomic fluctuation. Although threshold-exceeding deviations in order parameter (Figure 8B,C) seemed more widespread in the tertiary structure than for atomic fluctuation (Figure 7B,C), this might be attributed to the analysis being thresholded at the 10% level (as opposed to 50% in Figure 7). The lower threshold was introduced for the detection of local variations despite the sharper spikes. As with atomic fluctuation (Figure 7D), changes in VP55's order parameter upon association with VP39 (Figure 8D) appeared to be distributed throughout the protein, though they were much more focused in loops and β strands [as opposed to atomic fluctuation differences, which appeared to be localized predominantly in helices (Figure 7)]. In some instances, greater disorder was exhibited by VP55 alone, while in others, greater disorder was exhibited by VP39-associated VP55.

Possible Correlation of HDX with Langevin Dynamics Simulation. We attempted to find correlations between HDX and simulation data. Though the time scale of the simulation was nominally nanoseconds, the use of implicit solvent for modeling accompanied by a low frictional coefficient has previously allowed Langevin dynamics simulation to model events occurring on the microsecond to millisecond time scale (*28*, *29*), consistent with the experimental occurrence of individual HDX events on a time scale of tens of microseconds to milliseconds (*16*, *17*, *27*). Therefore, it did not seem inconceivable that a correlation might exist between simulation and experimentation. For the 28 peptic peptides in the VP55-alone data set whose full deuteration time course was available (see above and Table S1 of the Supporting Information), atomic fluctuation and order parameter values for the whole peptide were calculated as the mean of the per-residue values for the peptide's exchangeable residues divided by the mean for the whole of VP55. As with individual residues (Figure 6), simulated atomic fluctuation and order parameter for the peptides showed correlation (Figure 9A). Peptides in the extreme N-terminal region showed greater degrees of fluctuation for a given disorder than those in the remainder of VP55, as indicated with a separate line in Figure 9A. Apparently, this region, while relatively ordered, had a lower barrier to fluctuation during the simulation.

Finally, a search for correlations between HDX experimental data and Langevin dynamics simulation data for the 28 peptides was undertaken. A pattern emerged in which longer transition times (slower mean deuteration for a peptide) correlated with the observation of greater atomic fluctuation and greater disorder in the simulation. The relationship was most clearly observed after calculation of a "rates deviancy" score for the HDX experimental data, as a measure for concordance/discordance between HDX transition times and crystallographic SASA (see Experimental Procedures). Higher rates deviancy scores (approaching 100) indicated concordance between the transition time and predicted SASA for the amide proton (dashed line in Figure 3B), while lower scores indicate that the peptide was much more exchangeable than expected from its predicted SASA (ringed points in Figure 3B). When these scores are compared to simulation data, higher deviancy scores tended to correspond to greater simulated equilibrium atomic fluctuation (Figure 9B) and lower values to simulated order parameter [greater disorder (Figure 9C)]. In Figure 9B, as in Figure 9A, a steeper correlation was observed for peptides from the extreme N-terminal region of VP55 than for the other peptides, due to deviant values in this region for the simulated atomic fluctuation parameter.

The implication of the correlations observed in panels B and C of Figure 9 was that regions of the protein with lower-amplitude

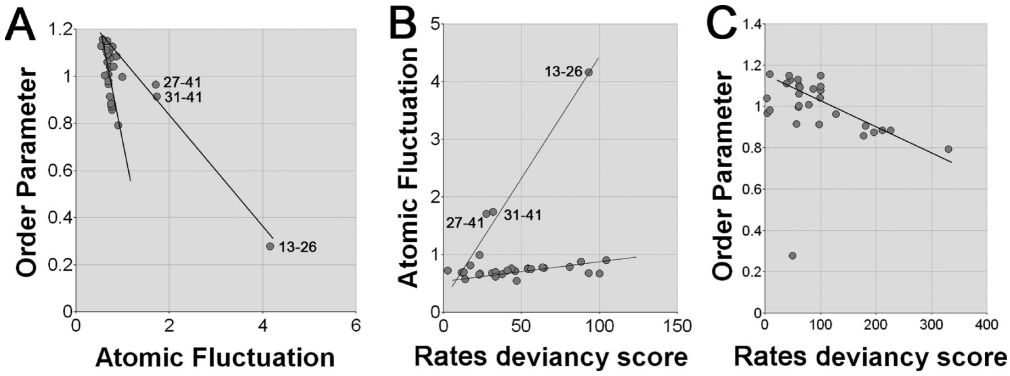

FIGURE 9: Possible correlation of HDX with Langevin dynamics simulation data for the set of 28 peptides (VP55-alone HDX experiments, all time points, see the text and Table 1). Linear regressions were added by eye, including a distinct regression for the three extreme N-terminal peptides. In panels B and C, the trend observed was not dependent upon the deuteration level employed for analysis. (A) Mean predicted atomic fluctutation vs order parameter for each of the 28 peptides. (B) Atomic fluctuation vs rates deviancy score (using a 64% deuteration level for calculating transition times). (C) Order parameter vs rates deviancy score (using a 95% deuteration level for calculating transition times).

simulated equilibrium backbone fluctuations and/or greater order tended to exchange amide protons at a rate faster than what would be expected from the calculated solvent exposure of the proton, whereas regions with more violent simulated vibration and/or greater disorder tended to be more dampened in exchange (exchanging more in proportion to solvent exposure of the proton).

DISCUSSION

Parameters for the LC-MALDI Method. Here, we have developed an LC-MALDI approach to HDX by mass spectrometry, which permitted HDX experiments to be performed in the context of peptide fractionation but without the use of dedicated (e.g., cooled) hardware attached to the mass spectrometer. This is a variant, or extension, of the MALDI-TOF MS approach HDX originally described by the Komives group and subsequently employed in a number of reports. The combination of HDX by MALDI-MS with rapid C18 chromatography has been reported (*30*), though only at the level of intact proteins, not peptides. It was used to dissociate an individual, intact protein from a protein complex prior to MALDI-TOF analysis of the dissociated protein; sites of exchange were not localized. In the study presented here, deuterated peptides were analyzed via LC-MALDI instead of LC-ESI-MS due to the instrumentation available in the authors' lab. MALDI seemed to present no clear disadvantages (discussed below). In addition to the nonrequirement for a dedicated mass spectrometer, minor advantages may also include the presence in mass spectra of just one charge state (+1) per ion and the slightly greater salt resistance claimed for MALDI (*31*).

Due to small intertime point and interexperiment variations in elution position for a given XIC (arising from slight changes in the backpressure in the capillary tip via use of a split flow system), the whole of each LC chromatogram was considered during XIC peak finding. It was not uncommon to find pairs of XIC peaks coincident in mass or with isotopic mass difference (give or take 30−40 ppm) and also indistinguishable in elution time (Table S1 of the Supporting Information), this despite XICs in which peptides eluted, typically, in just one to three fractions (3−9 s total) from the 132 fraction (∼400 s) gradient. These ambiguities were addressed at the software level (*32*). Coincidence of both measured mass and elution time might be a somewhat general issue in HDX studies that involve LC of peptic peptides of all but the smallest proteins, though the extent of this issue would clearly depend upon the mass accuracy and mass resolution of the mass analyzer, as well as LC peak resolution.

In this study, analyzed peptides (Table S1) covered 74% of the sequence of the target protein (VP55, a 55 kDa protein). This compared favorably with prior HDX studies using a nonfractionating MALDI approach, in which quantitative data for the extent of deuterium incorporation have been reported for 9−25 peptides covering 40−82% of the target protein sequence (*26*, *33*−*41*); however, in some instances, lower coverage was reported (*42*). In our nano-LC-MALDI approach, coverage represented a greater number of peptides (>82), leading to greater redundancy, with perhaps a greater emphasis on shorter peptides, permitting reasonable spatial resolution within the protein sequence. Moreover, the need to pick peptides based upon their presence in relatively clear areas of mass spectra was a less important concern with the nano-LC approach to MALDI due to resolution at the chromatographic level. Consequently, insofar as the complexity of the peptic peptide chromatogram may be expected to rise approximately with the square of protein chain length (assuming random pepsin action), the LC approach to HDX via MALDI would appear to have good potential for the analysis of larger proteins or protein complexes. This notwithstanding, our study represents only a preliminary proof of principle for the fractionating approach, and LC fractionation parameters could doubtless be optimized further.

For 28 of the peptic peptides of VP55, representing 40.1% sequence coverage, data were acquired at all 11 deuteration time points. The proportion of peptides for which all-time point data were obtained (28 of 119) seems comparable to that of other studies (*39*) and may compare favorably with those of HDX studies using a nonfractionating MALDI-MS approach. Typically, for nonfractionating MALDI-MS studies, between two and nine deuterium uptake rate curves have been shown and interpreted (*31*, *34*, *37*, *38*, *40*), though it is not clear whether additional, interpretable curves are available. A typical, recent ESI LC-MS analysis of deuterated peptides showed the full rate analysis of 29 peptides through all time points (*39*), equivalent to the number analyzed here. Coverage during our study was likely handicapped by the absence of denaturants during pepsinization, a step that has been used routinely in other laboratories (*39*, *41*) and has subsequently led to enhanced coverage during nano-LC-MALDI HDX studies of other proteins in the authors' lab (data not shown). Digestion variability in the absence of denaturants may have resulted in missing time points for a few of our peptides.

With regard to back-exchange, our overall analysis times from quench to spectral acquisition (12 min) were not dissimilar to those for the nonfractionating MALDI approach, the latter being on the order of 8.5 min (*39*); in other instances, up to 10 min was employed for pepsin digestion alone (*43*). The nano-LC-MALDI approach simplifies back-exchange calculations with respect to the nonfractionating approach, insofar as peptides are extracted from traces of deuterium that would otherwise favor the rapid, partial back-exchange of volatile groups [N- and C-termini and O-, N-, and S-containing side chains (*44*, *45*)] immediately after the quench step. In the nonfractionating MALDI approach, back-exchange levels for the nonvolatile backbone amides of peptic peptides have been reported to be between 21 and 46% (*26*, *34*−*39*, *41*, *42*, *46*). These levels of back-exchange have proven to be acceptable, even in experiments employing comparatively short deuterium uptake time points [e.g., 100 ms, 0.5 s, and 5 s (*43*)]. Comparable back-exchange rates were found in our nano-LC-MALDI experiments [∼36−41% (see above)], and in none of our time points did we see a collapse to the baseline of the % D parameter. Therefore, little or no detriment seems to have been associated with the addition of a peptide fractionation step to MALDI-MS-based HDX protocols. In other studies, exchange half-times of >1 h have been recorded for exposed peptide backbone amides at low temperatures and pH values (*45*), with HPLC solvents slowing the process further, so it was perhaps unsurprising that our ∼6−7 min separations were not associated with rampant back-exchange. Nonetheless, back-exchange levels in ESI-MS-based HDX studies may be somewhat more favorable (e.g., in ref *47*, an average back-exchange level of 15.3% was noted in the study of 61 peptides, varying from a minimum of 5.3% to a maximum of 25.1%).

Correlation of HDX Data with Protein Structural Parameters. Protection from amide proton exchange has been suggested to arise from hydrogen bonding and/or solvent exclusion (burying) of amide protons (*46*−*50*). In the latter regard, for example, HDX data generated via NMR have been correlated with SASA (*48*). HDX data generated via ESI-MS have also been correlated with structural parameters derived from crystallographic coordinates, including SASA, residue depth within the structure, and hydrogen bonding status (e.g., refs *44* and *49*, and references cited therein). HDX data generated via MALDI-MS have also been correlated with the structural parameters given above (*26*, *43*). In the latter reports, correlation was noted between numbers of deuterons incorporated and SASA values for whole amino acids or main chain atoms (*43*, *49*), as calculated using GETAREA (*50*) or the Connolly rolling ball method (*51*). In our study, crystallographic coordinates were used to calculate SASA values for the whole amino acid or for the amide proton alone (using a probe radius, 1.4 Å, comparable to that used in the prior studies). The resulting SASA values for each exchangeable position within a peptic peptide were summed across the peptide. As in the earlier studies, a mild correlation was observed between the proportion of protons within a peptide that resist rapid exchange and the SASA of the whole residue (Figure 1A). By contrast, there was no particular correspondence between HDX and SASA of the amide proton itself (Figure 1B). In fact, the extent of rapid exchange was generally greater than the line of proportionality with amide proton SASA, indicating less extensive amide protection in solution than was apparent from the heterodimer crystal structure. Exchange processes in solution may therefore be impacted by molecular dynamics considerations not apparent from the crystal structure alone, leading to the transient solvent exposure of internal regions of the protein on the time scale of HDX. Another interpretation might be that the solution conformation for VP55 is distinct from that in the heterodimer crystal.

Aside from SASA, a relationship between HDX and hydrogen bonding to the backbone amide proton has been considered in the interpretation of HDX-MS studies (*45*, *55*, *56*). Backbone amides support the network of hydrogen bonding and dipolar interactions upon which protein tertiary structure is generally based. A correlation has been noted between numbers of exchange-resistant amide protons in the peptic peptides of HDX-MS experiments and the extent of backbone amide hydrogen bonding as predicted from crystallographic coordinates (*43*). That study addressed a globular protein and a nonglobular protein, with a significantly higher correlation noted for the nonglobular protein (*43*). For VP55, however, which is considered to be globular, it was difficult to see an obvious correlation between HDX and hydrogen bonding (Figure 1C,D). There was, on average for the protein, more extensive exchange than what might be predicted from hydrogen bonding status. It is unclear whether this was related to dynamics (transient breakage of hydrogen bonds) or to a solution conformation for this protein distinct from that in the heterodimer crystal.

HDX and Molecular Dynamics Simulations. Combined HDX and molecular dynamics simulation approaches have been reported for several proteins (*52*, *53*). For example (*52*), HDX investigation of a kinase−substrate interaction was combined with normal-mode analysis (changes in potential energy around a minimum-energy conformation, approximated as a set of independent harmonic functions), quantifying the effects of simulated conformational fluctuation on the local environment around each residue via strain energy analysis (*54*). A localized correlation was observed between deuterium exchange rates and strain energy. In another study, the conformation of blood coagulation factor VIIa in the presence and absence of tissue factor was examined via a combination of HDX and molecular dynamics simulations of vibrational mean amplitudes (*53*) derived from crystallographic *B* factors and rmsd values. In that study, distances between side chain atoms were examined versus time using NAMD 2.5 (*55*) and the CHARMM22 force field for proteins (*56*). In a study of methylesterase cheB, deuterium incorporation corresponded quite well with the crystallographic *B* factor (*35*). As noted (*43*), theoretical studies have indicated that the density of contacts within a protein correlates with protections via HDX, as well as *B* factors and SASA (*57*, *58*). In a recent HDX study (*34*), an MD simulation was performed on the 213-amino acid protein (IκBα) and a mutant thereof in explicit solvent using an all-atom CHARMM force field, with initial coordinates based on the high-resolution structure of the cocrystal of IκBα in complex with NF-κB. Three separate 5 ns trajectories were followed for each protein, and significant rmsd's (between 2 and 4 Å) were found during the last 2 ns, around which structures fluctuated. The rmsd of each residue was calculated, and correlated motions were uncovered. However, it is not clear that a relationship was established between the simulation and HDX. Very recently, molecular dynamics simulations were used to establish the docking contacts of ligand in a combined molecular dynamics simulation/HDX study (*59*).

Here, we chose to perform a dynamics-based flexibility analysis (Langevin dynamics simulation) as opposed to a static structure-based approach (such as normal-mode analysis and *B* factor-based vibration analysis, etc.), since the dynamics-based

approach makes no assumptions regarding the type of motion (e.g., whether harmonic or nonharmonic). Instead, the system is simply represented according to classical molecular mechanics. In normal-mode analysis, by contrast, in addition to the classical molecular mechanics representation, a harmonic vibration is assumed at the bottom of the current local energy minimum. Similarly, a *B* factor-based vibration analysis does not rely on a classical molecular mechanics model, and reveals only harmonic vibrations at the local minimum (which in this case is taken to be the crystal structure). Further, in *B* factor fitting, uncertainty or insufficiency in measurement is incorporated into the *B* factor such that the latter contains information beyond atomic vibration. Moreover, crystal packing may also contribute [as noted by Truhlar et al. (*43*)], such that the vibration may relate only to the environment *in crystallo*. The major disadvantage of the Langevin dynamics simulation in our hands was a practical one, namely the requirement for several months of central processing unit time. After Langevin dynamics simulation with VP55 and the VP55−VP39 heterodimer, the whole VP55 molecule had re-equilibrated somewhat, the largest of the re-equilibrations occurring within VP55's N-terminal domain. At equilibrium, the most extreme atomic fluctuations were within the N- and C-terminal domains.

With regard to the possible correlation of HDX with Langevin dynamics simulations, it should be first noted that Langevin dynamics simulations, conducted on nominally nanosecond time scales, have successfully modeled events that have been shown to occur, experimentally, on time scales of microseconds to milliseconds (*28*, *29*). This was likely due to the use of implicit solvent for modeling in those studies, with a low solvent collision frequency (1 ps^{-1}). Since a solvent collision frequency of 1 ps^{-1} was also used in our study (Experimental Procedures), our simulation time scales are termed "nominally nanosecond", and we see no reason that we may not be modeling events occurring on much longer than nanosecond time scales, including the time scales of protein motion that regulate HDX with EX2 kinetics. In panels B and C of Figure 9, there appeared to be a negative correlation between backbone amide HDX propensity (positive deviation of HDX rate from linearity with amide proton's SASA) and either simulated atomic fluctuation or simulated disorder. The implication of this would be that HDX was actually retarded by the more violent of the simulated fluctuations, on the time scale of the simulation. HDX is considered to be very sensitive to conformational changes (interdomain and intradomain), global unfolding, and/or small-amplitude dynamic fluctuations, all of which may result in solvent penetration and/or hydrogen bond breakage (*16*, *27*, *60*). It has previously been demonstrated that an elevated internal energy of peptide ions in the gas phase leads to a significant decrease in the level of intermolecular hydrogen exchange (*61*). The negative correlation of HDX propensity with Langevin dynamics fluctuation and disorder in this study, in solution, seems to be consistent with this gas-phase observation. Another possibility might be that localized simulated dynamics were dominated by vibrational modes arising from the tertiary structure vibrating as a whole, and interconnected via its hydrogen bond network. Regions prone to such vibrations, therefore, would be those most rigidly connected to the whole body with least hydrogen bond disruption and opportunity for amide proton exchange.

Effect of VP39 on VP55. VP39 confers dramatic increases in processivity upon VP55 (*62*) and also changes VP55's mode of translocation upon single-stranded nucleic acid primer (*4*) with a concomitant rerouting of the primer around the VP55 polymerase (*11*). Crystal structures have been solved for the heterodimer and for VP39 alone (*6*, *8*), though the structure of VP55 alone has not been reported. In the Langevin dynamics simulations, docking of VP39 led to changes in the vibrational pattern and degree of disorder throughout VP55, though there was no evidence for whole-domain level changes in VP55 due to VP39 (Figure 7D) during the simulation. Likewise with HDX experiments, VP39-dependent changes in deuterium uptake by VP55 were demonstrated in various localized regions throughout VP55, but concentrated, large scale changes specific to a domain or surface were not observed, arguing against a dramatic, VP39-dependent conformational rearrangement in VP55. A net elevation of the apparent solvent accessibility was observed in a region of VP55's C-terminal domain whose ordered structure was previously shown to collapse upon primer binding (*11*). The structure of this C-terminal region may therefore change in accordance with the mode or stage of polymerase translocation, influenced by the VP39 subunit and/or primer. This would be the first clear function, to date, assigned to VP55's fairly sizable C-terminal domain. Nonetheless, the HDX data do not provide strong evidence of conformational changes upon formation of the VP55−VP39 heterodimer, as opposed to changes in the equilibria of existing protein dynamics. More precise definition of VP39-dependent structural changes awaits a crystal structure for VP55 alone (assuming this reflects VP55's solution structure) and/or HDX studies to record the effect of primer binding on HDX.

In conclusion, with HDX of VP55 alone, solvent accessibility and hydrogen bonding predicted from the VP55−VP39 heterodimer crystal structure could not consistently account for observed HDX rates, and inconsistencies in this regard were distributed throughout the tertiary structure of VP55. VP39 had a net, marginal cooling effect on VP55, indicating a possible restriction of VP55's flexibility in solution. VP39's cooling effect was most extensive within the central domain of VP55's three domains (notably the portion of this domain closest to VP39 in the crystal structure), while a patch within VP55's C-terminal domain showed an increased level of HDX in the presence of VP39. Consistent with HDX, simulation studies also indicated a slight cooling effect of VP39 upon VP55 with respect to order parameter, and again, simulated changes due to VP39 were distributed throughout VP55. Neither experiment nor simulation indicated that VP39 dramatically remodels the domains and/or interdomain relationships of VP55; rather, VP39 binding seems to lead to more modest changes dispersed throughout VP55.

SUPPORTING INFORMATION AVAILABLE

Additional data and discussion points. This material is available free of charge via the Internet at http://pubs.acs.org.

REFERENCES

1. Gershon, P. D., Ahn, B.-Y., Garfield, M., and Moss, B. (1991) Poly(A) polymerase and a dissociable polyadenylation stimulatory factor encoded by vaccinia virus. *Cell 66*, 1269–1278.
2. Gershon, P. D., and Moss, B. (1992) Transition from rapid processive to slow non-processive polyadenylation by vaccinia virus poly(A) polymerase catalytic subunit is regulated by the net length of the poly(A) tail. *Genes Dev. 6*, 1575–1586.

3. Johnson, L., Liu, S., and Gershon, P. D. (2004) Molecular flexibility and discontinuous translocation of a non-templated polymerase. *J. Mol. Biol. 337*, 843–885.
4. Yoshizawa, J., Li, C., and Gershon, P. D. (2007) Saltatory forward movement of a poly(A) polymerase during poly(A) tail addition. *J. Biol. Chem. 282*, 19144–19151.
5. Hodel, A. E., Gershon, P. D., and Quiocho, F. A. (1998) Structural basis for sequence non-specific recognition of 5′-capped mRNA by a cap modifying enzyme. *Mol. Cell 1*, 443–447.
6. Hodel, A. E., Gershon, P. D., Shi, X., and Quiocho, F. A. (1996) The 1.85 Å structure of vaccinia protein VP39: A bifunctional enzyme that participates in the modification of both mRNA ends. *Cell 85*, 247–256.
7. Johnson, L., and Gershon, P. D. (1999) RNA binding characteristics and overall topology of the vaccinia poly(A) polymerase-processivity factor complex. *Nucleic Acids Res. 27*, 2708–2721.
8. Moure, C. M., Bowman, B. R., Gershon, P. D., and Quiocho, F. A. (2006) Crystal structures of the vaccinia virus polyadenylate polymerase heterodimer: Insights into ATP selectivity and processivity. *Mol. Cell 33*, 339–349.
9. Deng, J., Ernst, N. L., Turley, S., Stuart, K. D., and Hol, W. G. (2005) Structural basis for UTP specificity of RNA editing TUTases from *Trypanosoma brucei*. *EMBO J. 24*, 4007–4017.
10. Deng, L., Beigelman, L., Matulic-Adamic, J., Karpeisky, A., and Gershon, P. D. (1997) Specific recognition of an rU_2-N_{15}-rU motif by VP55, the vaccinia virus poly(A) polymerase catalytic subunit. *J. Biol. Chem. 272*, 31542–31552.
11. Li, C.-Z., Li, H., Zhou, S.-F., Sun, E., Yoshizawa, J., Poulos, T. L., and Gershon, P. D. (2009) Polymerase translocation with respect to single-stranded nucleic acid: Looping or wrapping of primer around a poly(A) polymerase. *Structure 17*, 1–10.
12. Hodel, A. E., Gershon, P. D., Shi, X., Wang, S.-M., and Quiocho, F. A. (1997) Specific protein recognition of an mRNA cap through its alkylated base. *Nat. Struct. Biol. 4*, 350–354.
13. Linderstrøm-Lang, K. (1952) Lane Medical Lectures. In Proteins and Enzymes, Stanford University Press, Palo Alto, CA.
14. Hvidt, A., and Nielsen, S. O. (1966) Hydrogen exchange in proteins. *Adv. Protein Chem. 21*, 287–386.
15. Englander, S. W., Sosnick, T. R., Englander, J. J., and Mayne, L. (1996) Mechanisms and uses of hydrogen exchange. *Curr. Opin. Struct. Biol. 6*, 18–23.
16. Hoofnagle, A. N., Resing, K. A., and Ahn, N. G. (2003) Protein analysis by hydrogen exchange mass spectrometry. *Annu. Rev. Biophys. Biomol. Struct. 32*, 1–25.
17. Wales, T. E., and Engen, J. R. (2006) Hydrogen exchange mass spectrometry for the analysis of protein dynamics. *Mass Spectrom. Rev. 25*, 158–170.
18. Perkins, D. N., Pappin, D. J. C., Creasy, D. M., and Cottrell, J. S. (1999) Probability-based protein identification by searching sequence databases using mass spectrometry data. *Electrophoresis 20*, 3551–3567.
19. Nikamanon, P., Pun, E., Chou, W., Koter, M., and Gershon, P. D. (2008) "TOF2H": A precision toolbox for rapid, high density/high coverage hydrogen-deuterium exchange mass spectrometry via an LC-MALDI approach, covering the data pipeline from spectral acquisition to HDX rate analysis. *BMC Bioinf. 9*, 387.
20. Guvench, G., and Brooks, C. L., III (2004) Efficient approximate all-atom solvent accessible surface area method parameterized for folded and denatured protein conformations. *J. Comput. Chem. 25*, 1005–1014.
21. Fiser, A., Do, R. K., and Sali, A. (2000) Modeling of loops in protein structures. *Protein Sci. 9*, 1753–1773.
22. Sali, A., and Blundell, T. L. (1993) Comparative protein modelling by satisfaction of spatial restraints. *J. Mol. Biol. 234*, 779–815.
23. Marti-Renom, M. A., Stuart, A., Fiser, A., Sánchez, R., Melo, F., and Sali, A. (2000) Comparative protein structure modeling of genes and genomes. *Annu. Rev. Biophys. Biomol. Struct. 29*, 291–325.
24. Ryckaert, J. P., Ciccotti, G., and Berendsen, H. J. C. (1977) Numerical-Integration of Cartesian Equations of Motion of a System with Constraints: Molecular Dynamics of N-Alkanes. *J. Comput. Phys. 23*, 327–341.
25. Hockney, R. W., and Eastwood, J. W. (1981) Computer Simulations Using Particles, McGraw-Hill, New York.
26. Truhlar, S. M. E., Torpey, J. W., and Komives, E. A. (2006) Regions of IκBα that are critical for its inhibition of NF-κB DNA interaction fold upon binding to NF-κB. *Proc. Natl. Acad. Sci. U.S.A. 103*, 18951–18956.
27. Englander, S. W., and Kallenbach, N. (1984) Hydrogen exchange and structural dynamics of proteins and nucleic acids. *Q. Rev. Biophys. 16*, 521–655.
28. Ishima, R., Freedberg, D. I., Wang, Y. X., Louis, J. M., and Torchia, D. A. (1999) Flap opening and dimer-interface flexibility in the free and inhibitor-bound HIV protease, and their implications for function. *Structure 7*, 1047–1055.
29. Hornak, V., Okur, A., Rizzo, R. C., and Simmerling, C. (2006) HIV-1 protease flaps spontaneously open and reclose in molecular dynamics simulations. *Proc. Natl. Acad. Sci. U.S.A. 103*, 915–920.
30. Nazabal, A., and Schmitter, J.-M. (2006) Hydrogen-deuterium exchange analyzed by matrix-assisted laser desorption-ionization mass spectrometry and the HET-s prion model. *Methods Enzymol. 413*, 167–181.
31. Tuma, R., Coward, L., Kirk, M., Barnes, S., and Prevelige, P. J. (2001) Hydrogen-deuterium exchange as a probe of folding and assembly in viral capsids. *J. Mol. Biol. 306*, 389–396.
32. Cauich, E., and Gershon, P. D. (2009) Two new tools for applying chromatographic retention data to the mass-identification of HDX peptides during HD-exchange experiments by nanoLC-MALDI. 57th ASMS Conference on Mass Spectrometry and Allied Topics, Philadelphia, May 31−June 4, 2009, Wednesday Poster 420.
33. Betts, G. N., van der Geer, P., and Komives, E. A. (2008) Structural and functional consequences of tyrosine phosphorylation in the LRP1 cytoplasmic domain. *J. Biol. Chem. 283*, 15656–15664.
34. Ferreiro, D. U., Cervantes, C. F., Truhlar, S. M. E., Cho, S. S., Wolynes, P. G., and Komives, E. A. (2007) Stabilizing IκBα by "Consensus" Design. *J. Mol. Biol. 365*, 1201–1216.
35. Hughes, C. A., Mandell, J. G., Anand, G. S., Stock, A. M., and Komives, E. A. (2001) Phosphorylation causes subtle changes in solvent accessibility at the interdomain interface of methylesterase CheB. *J. Mol. Biol. 307*, 967–976.
36. Hughes Croy, C., Bergqvist, S., Huxford, T., Ghosh, G., and Komives, E. A. (2004) Biophysical characterization of the free IκBα ankyrin repeat domain in solution. *Protein Sci. 13*, 1767–1777.
37. Anand, G. S., Law, D., Mandell, J. G., Snead, A. N., Tsigelny, I., Taylor, S. S., Ten Eyck, L. F., and Komives, E. A. (2003) Identification of the protein kinase A regulatory RI -catalytic subunit interface by amide H 2H exchange and protein docking. *Proc. Natl. Acad. Sci. U.S.A. 100*, 13264–13269.
38. Koeppe, J. R., and Komives, E. A. (2006) Amide H/2H exchange reveals a mechanism of thrombin activation. *Biochemistry 45*, 7724–7732.
39. Shi, J., Koeppe, J. R., Komives, E. A., and Taylor, P. (2006) Ligand-induced conformational changes in the acetylcholine-binding protein analyzed by hydrogen-deuterium exchange mass spectrometry. *J. Biol. Chem. 281*, 12170–12177.
40. Mandell, J. G., Baerga-Ortiz, A., Akashi, S., Takio, K., and Komives, E. A. (2001) Solvent accessibility of the thrombinthrombomodulin interface. *J. Mol. Biol. 306*, 575–589.
41. Anand, G. S., Hughes, C. A., Jones, J. M., Taylor, S. S., and Komives, E. A. (2002) Amide H/2H exchange reveals communication between the cAMP and catalytic subunit-binding sites in the RIa subunit of protein kinase A. *J. Mol. Biol. 323*, 377–386.
42. Croy, C. H., Koeppe, J. R., Bergqvist, S., and Komives, E. A. (2004) Allosteric changes in solvent accessibility observed in thrombin upon active site occupation. *Biochemistry 43*, 5246–5255.
43. Truhlar, S. M., Croy, C. H., Torpey, J. W., Koeppe, J. R., and Komives, E. A. (2006) Solvent accessibility of protein surfaces by amide H/2H exchange MALDI-TOF mass spectrometry. *J. Am. Soc. Mass Spectrom. 17*, 1490–1497.
44. Yan, X., Watson, J., Ho, P. S., and Deinzer, M. L. (2004) Mass spectrometric approaches using electrospray ionization charge states and hydrogen−deuterium exchange for determining protein structures and their conformational changes. *Mol. Cell. Proteomics 3*, 10–23.
45. Englander, J. J., Rogero, J. R., and Englander, S. W. (1985) Protein Hydrogen Exchange Studied by the Fragment Separation Method. *Anal. Biochem. 147*, 234–244.
46. Gertsman, I., Gan, L., Guttman, M., Lee, K., Speir, J., Duda, R., Hendrix, R., Komives, E., and Johnson, J. (2009) An unexpected twist in viral capsid maturation. *Nature 458*, 646–650.
47. Yan, X., Broderick, D., Leid, M. E., Schimerlik, M. I., and Deinzer, M. L. (2004) Dynamics and Ligand-Induced Solvent Accessibility Changes in Human Retinoid X Receptor Homodimer Determined by Hydrogen Deuterium Exchange and Mass Spectrometry. *Biochemistry 43*, 909–917.
48. Jeng, M.-F., and Dyson, H. J. (1995) Comparison of the hydrogen-exchange behavior of reduced and oxidized *Escherichia coli* thioredoxin. *Biochemistry 34*, 611–619.
49. Yan, X., Zhang, H., Watson, J., Schimerlik, M. I., and Deinzer, M. L. (2002) H/D exchange and mass spectrometric analysis of a protein

containing multiple disulfide bonds: Solution structure of recombinant macrophage colony stimulating factor-β (rhM-CSF). *Protein Sci. 11*, 2113–2124.
50. Fraczkiewicz, R., and Wraun, B. (1998) Exact and efficient analytical calculation of the accessible surface areas and their gradients for macromolecules. *J. Comput. Chem. 19*, 319–19333.
51. Connolly, M. L. (1983) Solvent-accessible surfaces of proteins and nucleic acids. *Science 221*, 709–713.
52. Wong, L., Lieser, S. A., Miyashita, O., Miller, M., Tasken, K., Onuchic, J. N., Adams, J. A., Woods, V. L., and Jennings, P. A. (2005) Coupled Motions in the SH2 and Kinase Domains of Csk Control Src Phosporylation. *J. Mol. Biol. 351*, 131–143.
53. Olsen, O. H., Rand, K. D., Østergaard, H., and Persson, E. (2007) A combined structural dynamics approach identifies a putative switch in factor VIIa employed by tissue factor to initiate blood coagulation. *Protein Sci. 16*, 671–682.
54. Miyashita, O., Onuchic, J. N., and Wolynes, P. G. (2003) Nonlinear elasticity, proteinquakes, and the energy landscapes of functional transitions in proteins. *Proc. Natl. Acad. Sci. U.S.A. 100*, 12570–12575.
55. Gullingsrud, J., and Schulten, K. (2003) Gating of MscL studied by steered molecular dynamics. *Biophys. J. 85*, 2087–2099.
56. McKerell, A. D., Jr., Bashford, D., Bellott, M., Dunbrack, R. L., Jr., Evanseck, J., Field, M. J., Fisher, S., Gao, J., Guo, H., and Ha, S.; et al. (1998) All-hydrogen empirical potential for molecular modelling and dynamics studies of proteins using the CHARMM22 force field. *J. Phys. Chem. 102*, 3586–3616.
57. Shoemaker, B. A., Wang, J., and Wolynes, P. G. (1999) Exploring Structures in Protein Folding Funnels with Free Energy Functional: The Transition State Ensemble. *J. Mol. Biol. 287*, 675–694.
58. Shoemaker, B. A., and Wolynes, P. G. (1999) Exploring Structures in Protein Folding Funnels with Free Energy Functionals: The Denatured Ensemble. *J. Mol. Biol. 287*, 657–674.
59. Burke, J. E., Babakhani, A., Gorfe, A. A., Kokotos, G., Li, S., Woods, V. L., Jr., McCammon, J. A., and Dennis, E. A. (2009) Location of Inhibitors Bound to Group IVA Phospholipase A2 Determined by Molecular Dynamics and Deuterium Exchange Mass Spectrometry. *J. Am. Chem. Soc. 131*, 8083–8091.
60. Johnson, R., and Walsh, K. (1994) Mass-spectrometric measurement of protein amide hydrogen-exchange rates of apo-myoglobin and holo-myoglobin. *Protein Sci. 3*, 2411–2418.
61. Kaltashov, I. A., Doroshenko, V. M., and Cotter, R. J. (1997) Gas phase-hydrogen/deuterium exchange reactions of peptide ions in a quadrupole ion trap mass spectrometer. *Proteins: Struct., Funct., Genet. 28*, 53–58.
62. Gershon, P. D., and Moss, B. (1993) Stimulation of poly(A) tail elongation by the VP39 subunit of the vaccinia virus-encoded poly(A) polymerase. *J. Biol. Chem. 268*, 2203–2210.
63. Bai, Y., Milne, J. S., Mayne, L., and Englander, S. W. (1993) Primary structure effects hydrogen exchange on peptide group. *Proteins: Struct., Funct., Genet. 17*, 75–86.